

Counter-rotating eddy pair in the Luzon Strait

Sun Ruili^{1,2*}, Li Peiliang^{1,3}, GuYanzhen³, Zhai Fangguo⁴, Yan Yunwei², Li Bo⁵, Zhang Yang²

¹Hainan Institute of Zhejiang University, Sanya, Hainan, China

²State Key Laboratory of Satellite Ocean Environment Dynamics, Second Institute of Oceanography, Ministry of Natural Resources, Hangzhou, China

³Ocean college, Zhejiang University, Zhoushan, China

⁴College of Oceanic and Atmospheric Sciences, Ocean University of China, Qingdao, China

⁵State Key Laboratory of Tropical Oceanography, South China Sea Institute of Oceanology, Chinese Academy of Sciences, Guangzhou, China

Corresponding author: Sun Ruili, sunruili2007@126.com

Abstract:

Based on satellite remote-sensing observation data and Hybrid Coordinate Ocean Model (HYCOM) re-analysis data, we studied the counter-rotating eddy pair in the Luzon Strait (LS). Statistical analysis reveals that when an anti-cyclonic mesoscale eddy (AE) (cyclonic mesoscale eddy [CE]) in the Northwest Pacific (NWP) gradually approaches the east side of the LS, a CE (an AE) gradually forms on the west side of the LS, and it is defined as the AE (CE) mode of the counter-rotating eddy pair in the LS. The counter-rotating eddy pair exhibits obvious seasonal variation: the AE mode mainly occurs in the summer half of the year, while the CE mode mainly occurs in the winter half of the year. The mean durations of the AE and CE modes are both approximately 70 day (d). Based on vorticity budget equation and energy analysis, the dynamic mechanism of counter-rotating eddy-pair occurrence is determined to be as follows: the AE (CE)

23 on the east side of the LS causes a positive (negative) vorticity anomaly through horizontal
24 velocity shear on the west side of the LS, and the positive (negative) vorticity anomaly is
25 transported westward by the zonal advection of the vorticity, finally leading to the formation of the
26 CE (AE) on the west side of the LS.

27 **Keywords:** counter-rotating eddy pair; Luzon Strait; vorticity budget equation; barotropic
28 instability

29 **1 Introduction**

30 The Luzon Strait (LS), located between the island of Taiwan and Luzon Island, is an important
31 gap for particle and energy exchange between the South China Sea (SCS) and Northwest Pacific
32 (NWP). The topography around the LS is very complicated. The LS is composed of three straits
33 from north to south: Bashi Strait, Balintang Strait, and Babuyan Strait. The Batanes Islands and
34 Babuyan Islands are located in these straits (Figure 1). This complex topography leads to the
35 generation and aggregation of a large number of mesoscale eddies, which then play an important
36 role in the dynamic ocean process around the LS (Liu *et al.*, 2012; Lu and Liu, 2013; Sun *et al.*,
37 2016a; Sun *et al.*, 2020).

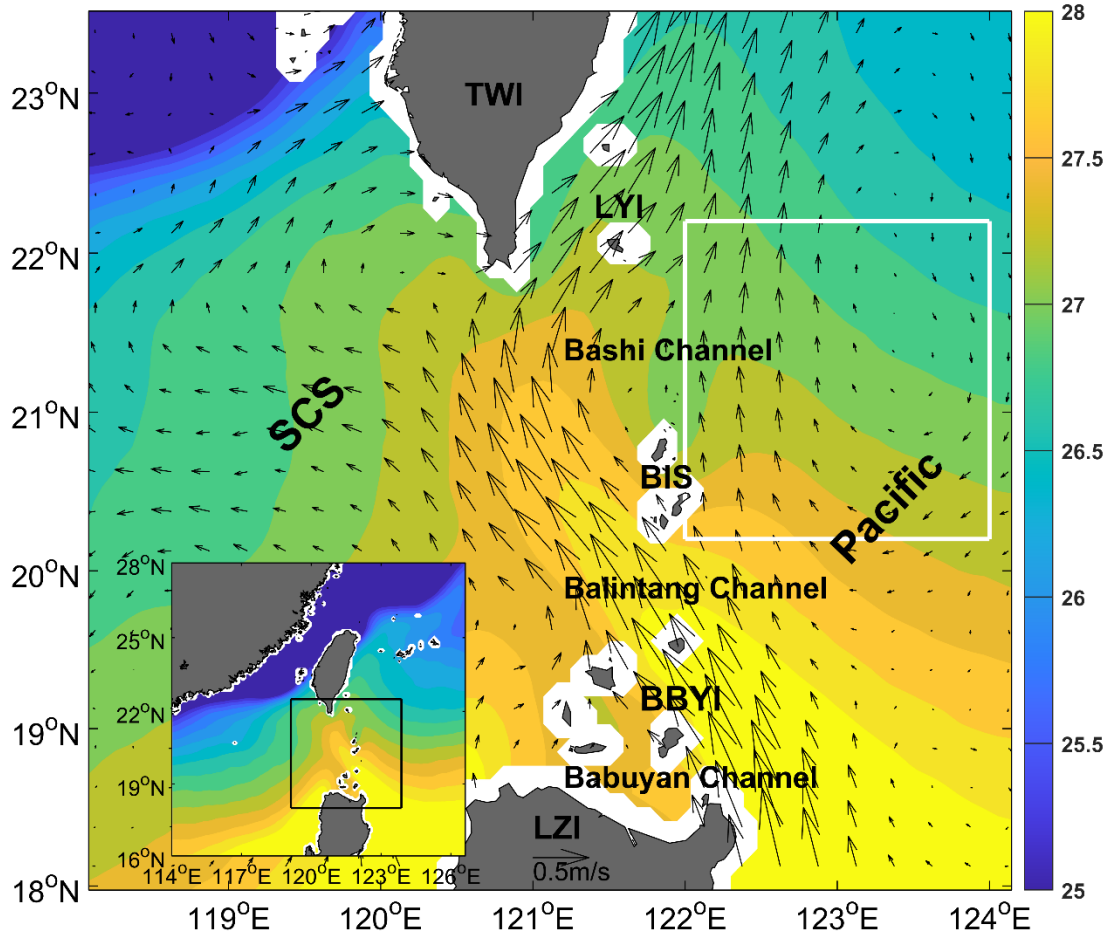
38 Mesoscale eddies interaction is an important focus of previous studies on mesoscale eddies in
39 the LS. Jing and Li (2003) used satellite remote-sensing observation data to discover a cyclonic
40 mesoscale cold eddy around Lanyu Island to the northeast of the LS. They pointed out that the
41 formation of the Lanyu cold eddy was the result of the joint action of the meandering Kuroshio
42 overshooting and conservation of the potential vorticity. Sun *et al.* (2016b) believed that the
43 formation of the Lanyu cold eddy was a process of eddies-eddies interaction. They used satellite
44 observation data and composition analysis to study the Lanyu cold-eddy phenomenon, and pointed

45 out that the combined action of the Kuroshio loop (cyclonic circulation) and an AE from the NWP
46 leading to the formation of the Lanyu cold eddy. Based on satellite observation data, *in situ*
47 observation data and numerical modelling data, Zhang *et al.* (2017) studied mesoscale
48 eddies-eddies interaction to the northwest of the LS. They analyzed the energy budget of the
49 Kuroshio invading the SCS, and determined that the northern branch of the anti-cyclonic
50 circulation caused by the Kuroshio loop had a large horizontal shear stress and thus led to the
51 formation of a CE southwest of Taiwan Island through the barotropic instability.

52 Previous studies showed that mesoscale eddies-eddies interaction can cause particle and
53 energy exchange and often occurs in the vicinity of the LS (Sun *et al.*, 2016b; Zhang *et al.*, 2017;
54 Sun *et al.*, 2018). Since the LS is an important gap for particle and energy exchange between the
55 SCS and NWP, a logical question is whether this phenomenon of mesoscale eddies-eddies
56 interaction can occur on the east and west sides of the LS and whether it plays an important role in
57 the particle and energy exchange between the SCS and NWP. To explore this issue, we compare
58 sea-surface height anomaly (SSHA) distributions in the SCS when a CE occurs and when an AE
59 occurs on the east side of the LS (Figure 2). The specific process is described in detail in Section
60 3.1. Figure 2 shows that when an AE (a CE) occurs on the east side of the LS, a CE (an AE) forms
61 on the west side of the LS, which was observed in the in-situ observation data (Huang *et al.*, 2019).
62 This is referred to in this article as the counter-rotating eddy-pair phenomenon.

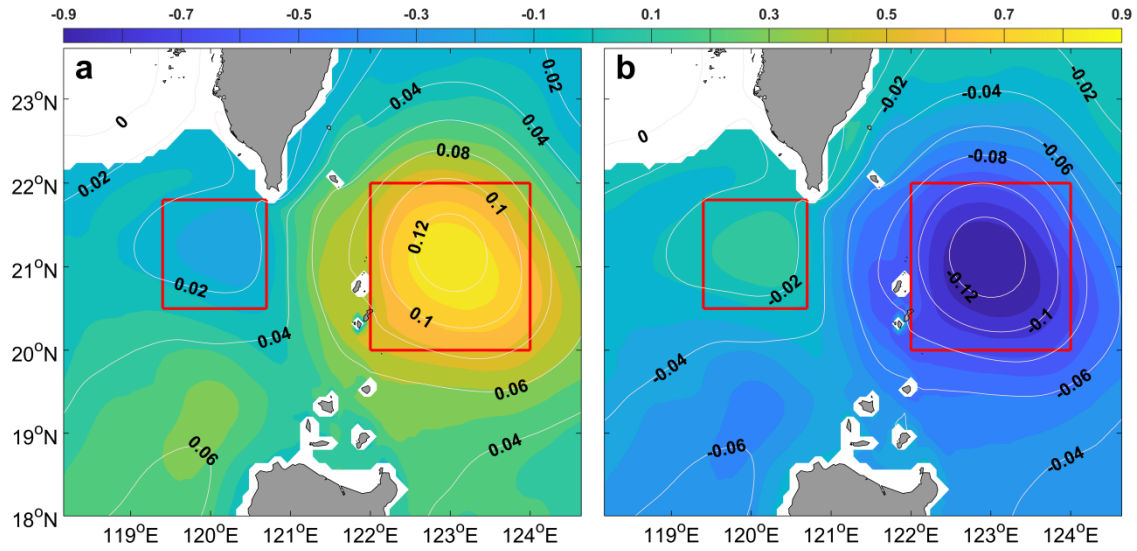
63 To our knowledge, this is the first time a counter-rotating eddy-pair phenomenon in the LS
64 has been proposed, which creates a new form of particle and energy exchange between the SCS
65 and the NWP. The present study will supplement and fulfill the theory of particle and energy
66 exchange between the SCS and NWP. We give the statistical characteristics and dynamic

67 mechanism of this phenomenon herein. The rest of this paper is organized as follows. Section 2
 68 briefly introduces the data and methods, Section 3 presents the research results, and Section 4
 69 provides a discussion and conclusion.



70
 71 Figure 1. Climate state of spatial distribution of Remote Sensing Systems (RSS) SST (°C; shading)
 72 and CMEMS geostrophic current (m/s; vectors) from 2003 to 2020. SCS, South China Sea; BIS,
 73 Batanes Islands; TWI, Taiwan Island; LZI, Luzon Island; BBYI, Babuyan Islands; LYI, Lanyu
 74 Island. White box borders 20.2–22.2°N, 122–124°E. Extent of the main map is shown as
 75 black-bordered box in inset.

76



77

78 Figure 2. Spatial distribution of counter-rotating eddy pair in the LS. Spatial patterns of AE (a) and
 79 CE (b) modes. Panel a (b) corresponds to average state when an AE (a CE) occurred in area
 80 marked by red box on east side of LS from 1993 to 2020. Contours represent SSHA (units of m).
 81 Colors represent sea temperature anomaly (units of °C) at a depth of 300 m. Interval of SSHA is
 82 0.03 m. Red boxes on west and east sides of LS border mark 20.5–21.8°N, 119.4–120.7°E and 20–
 83 22°N, and 122–124°E, respectively. Figure is similar to Figure 3 of Sun *et al.* (2018), and is based
 84 on HYCOM data.

85 2 Data and methods

86 2.1 Data

87 Satellite remote-sensing SSHA, geostrophic current, and geostrophic current anomaly data
 88 were provided by the Copernicus Marine Environment Monitoring Service (CMEMS). The dataset
 89 was generated by the processing system including data from all altimeter missions: Sentinel-3A/B,
 90 Jason-3, HY-2A, Cryosat-2, OSTM/Jason-2, Jason-1, Topex/Poseidon, Envisat, GFO, and
 91 ERS-1/2. The dataset provides global coverage data from January 1, 1993 to August 2, 2021, with
 92 a spatial resolution of 0.25°×0.25° and temporal sampling frequency of 1 d. It also provides one

93 near-real-time component and one delayed-time component. The delayed-time component has
94 been inter-calibrated and provides a homogeneous and highly accurate, long time series of all
95 altimeter data (Pujol and Françoise, 2019), and is chosen for use in this paper.

96 Model data are obtained from the Hybrid Coordinate Ocean Model (HYCOM) model output
97 by the U.S. Naval Research Laboratory. The dataset is based on ocean prediction system output,
98 and the product with the longest time span from 2 October 1992 to 31 December 2012 was chosen
99 from all HYCOM data-assimilation products provided by the HYCOM organization. The dataset
100 is based on ocean prediction system output with a spatial resolution of $0.08^\circ \times 0.08^\circ$ and 40
101 standard z levels between 80.48°S and 80.48°N . It provides temperature, salinity, sea-surface
102 height, zonal flow, and meridional flow (Wallcraft *et al.*, 2003).

103 The wind dataset was provided by the National Centers for Environmental Information
104 (NCEI). The dataset merges multiple satellite observations with *in situ* instrument and related
105 individual products, provides 6-h, daily, and monthly wind and climate data with a spatial
106 resolution of $0.25^\circ \times 0.25^\circ$, and contains globally gridded ocean surface vector winds and wind
107 stresses (Zhang *et al.*, 2006).

108 Sea surface temperature (SST) data are from remote-sensing systems (RSSs). The dataset
109 merges the near-coastal capability and high spatial resolution of infrared SST data with
110 through-cloud capabilities of microwave SST data, and has applied atmospheric corrections. It
111 provides daily data with a spatial resolution of $9\text{ km} \times 9\text{ km}$ from July 1, 2002 to the present.

112 2.2 Methods

113 2.2.1 Eddy energetic and hydrodynamic instability formula

114 The formation mechanisms of mesoscale eddies in the ocean are commonly attributed to

115 baroclinic and barotropic instabilities (Pedlosky, 1987). The barotropic conversion (BT) and
 116 baroclinic conversion (BC) are manifestations of the baroclinic and barotropic instabilities,
 117 respectively, and they are the major eddy energy sources around the LS (Yang *et al.*, 2013; Zhang
 118 *et al.*, 2013, 2015, 2017). In addition, the wind-stress work (WW) can also contribute to the
 119 formation of eddies (Ivchenko, 1997; Sun *et al.*, 2015). The BT, BC, and WW can be expressed as
 120 follows (Ivchenko, 1997; Oey, 2008):

$$121 \quad BT = - \int \left(\overline{u'^2 \frac{\partial \bar{u}}{\partial x}} + \overline{v'^2 \frac{\partial \bar{v}}{\partial y}} + \overline{u' v' \frac{\partial \bar{u}}{\partial y}} + \overline{u' v' \frac{\partial \bar{v}}{\partial x}} \right) dz, \quad (1)$$

$$122 \quad BC = - \int \frac{g^2}{\rho_0^2 N^2} \left(\overline{u' \rho' \frac{\partial \bar{\rho}}{\partial x}} + \overline{v' \rho' \frac{\partial \bar{\rho}}{\partial y}} \right) dz, \quad (2)$$

$$123 \quad WW = \frac{1}{\rho} \left(\overline{u' \tau'_x} + \overline{v' \tau'_y} \right), \quad (3)$$

124 Where t is time; u, v , and w are the zonal velocity, meridional velocity, and vertical velocity,
 125 respectively, and their positive directions are east, north, and up, respectively. g is the
 126 acceleration due to gravity; N is the buoyancy frequency; ρ is the density of sea water; $\rho_0 =$
 127 $1030 \text{ kg} \cdot \text{m}^{-3}$ is the mean sea-water density; p is the sea pressure; and τ_x and τ_y are the zonal
 128 and meridional components of the wind stress, respectively. x, y , and z are the conventional
 129 east-west, north-south, and up-down Cartesian coordinates, respectively. The depth integrals for
 130 BT and BC are from 400 m to the sea surface. The overbar denotes a time average over 70 d, the
 131 primes denote deviations from the average value of 35 d before and after this day, and the other
 132 symbols and notations are standard. From Figures 6 and 8, it can be seen that the counter-rotating
 133 eddy-pair phenomenon occurs, develops, and disappears from $t = -36$ to $t = 36$, i.e., approximately
 134 70 d. Therefore, the period is chosen to be 70 d. We have made several attempts to set the period
 135 between 65 and 80 d, and they will not affect our basic conclusion. BT and BC were calculated
 136 from HYCOM data. CMEMS surface-current velocity data and NCDC wind data were used to

137 calculate WW.

138 2.2.2 Vorticity budget equation

139 To examine the influence of the vorticity change, we applied the vorticity budget equation

140 (Muller,1995; Kuo and Tseng, 2021):

$$141 \quad \frac{\partial \zeta}{\partial t} = -u \frac{\partial \zeta}{\partial x} - v \frac{\partial \zeta}{\partial y} - (\zeta + f) \nabla \cdot \vec{u} - v \frac{\partial f}{\partial y} + \frac{1}{\rho^2} \left(\frac{\partial \rho}{\partial x} \frac{\partial P}{\partial y} - \frac{\partial \rho}{\partial y} \frac{\partial P}{\partial x} \right) - v \frac{\partial^2 \zeta}{\partial z^2}, \quad (4)$$

142 Where $\zeta = \frac{\partial v}{\partial x} - \frac{\partial u}{\partial y}$ is the relative vorticity, t is time, f is the Coriolis parameter, P is the

143 sea-water pressure, and $\nu = 1.004 \times 10^{-6}$ is the kinematic viscosity coefficient.

144 x, y, z, u, v , and ρ in formula (4) are defined as in formulas (1)-(3). The items on the right-hand

145 side of the equation are, from left to right, the zonal advection, meridional advection, stretching,

146 beta, baroclinic, and diffusion terms.

147 2.2.3 Definition of modes and intensity index of counter-rotating eddy-pair phenomenon

148 When an AE (a CE) in the NWP gradually approaches the northern LS, a CE (an AE)

149 gradually forms on the west side of the LS, and we define it as an AE (a CE) mode of the

150 counter-rotating eddy-pair phenomenon, as shown in Figures 2a, 3a, and 6 (Figures 2b, 3b, and 8).

151 To reflect the intensity of counter-rotating eddy-pair phenomenon, we must construct an

152 intensity index. As this phenomenon mainly involves the difference of SSHA between the east and

153 west sides of the LS, the index is defined as the time series of the SSHA in the east red box of

154 Figure 2 (expressed as $SSHA_{east}$) minus that in the west red box of Figure 2 (expressed as $SSHA_{west}$),

155 which is shown in Figure 3a and can be expressed as $Index = SSHA_{east} - SSHA_{west}$.

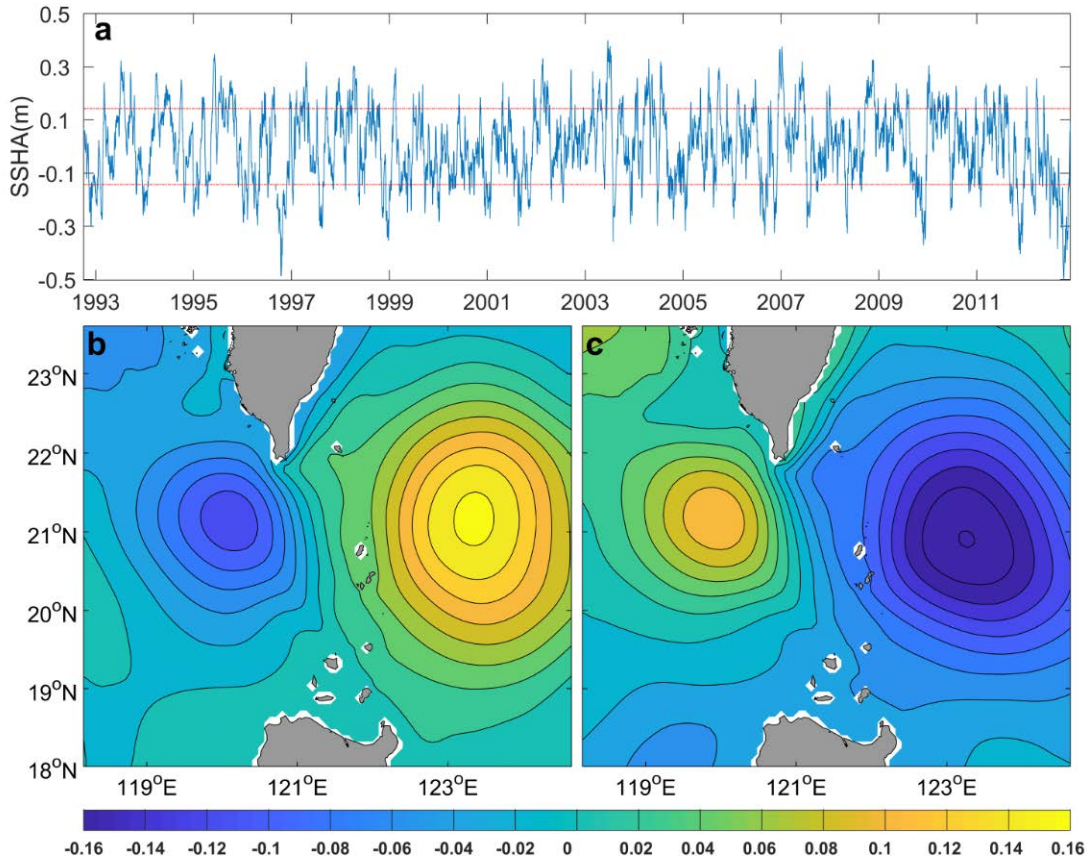
156 3 Results

157 3.1 Identification of counter-rotating eddy pair in LS

158 Based on cluster analysis, which is the same as the clustering method used by Sun *et al.*

159 (2018), the SSHA and sea-temperature anomaly (STA) are determined based on the days when an
160 AE and a CE exist on the east side of the LS (shown in the white box in Figure 1), respectively.
161 Figure 2a shows that the SSHA in the red box on the east side of the LS increases from the outside
162 to inside, which means that there is an AE. Owing to geostrophic balance and mass conservation,
163 the AE causes convergence of sea water, leading to down-welling in its center, subsequently
164 leading to an increase in the temperature in the deep ocean. This is verified by the fact that the
165 STA in the red box on the east side of the LS gradually increases from outside to inside and the
166 value is highest in the center. In addition, the SSHA in the red box on the west side of the LS
167 decreases from outside to inside and the STA is negative, indicating the presence of a weak CE.
168 According to the definition of modes of the counter-rotating eddy pair given in Section 2.2.3, the
169 SSHA pattern in Figure 2a can be identified as an AE mode of the counter-rotating eddy pair.

170 Figure 2b is similar to Figure 2a, but for a CE and an AE on the east and west sides of the LS,
171 respectively, its SSHA pattern can be identified as an AE mode of the counter-rotating eddy pair.
172 According to the intensity index defined in Section 2.2.3, the SSHA is constructed based on the
173 days when the positive and negative intensity index values are more than one standard deviation
174 from the mean, as shown in Figures 3b and 3c. Figure 3b (3c) shows that an AE (a CE) on the east
175 side of the LS corresponds well to a CE (an AE) on the west side of the LS, and can well reflect
176 the AE (CE) mode of a counter-rotating eddy pair in the LS. It also shows that we can well
177 identify this phenomenon according to the intensity index, and, furthermore, that the positive and
178 negative intensity indexes correspond to AE and CE modes, respectively, of this phenomenon.



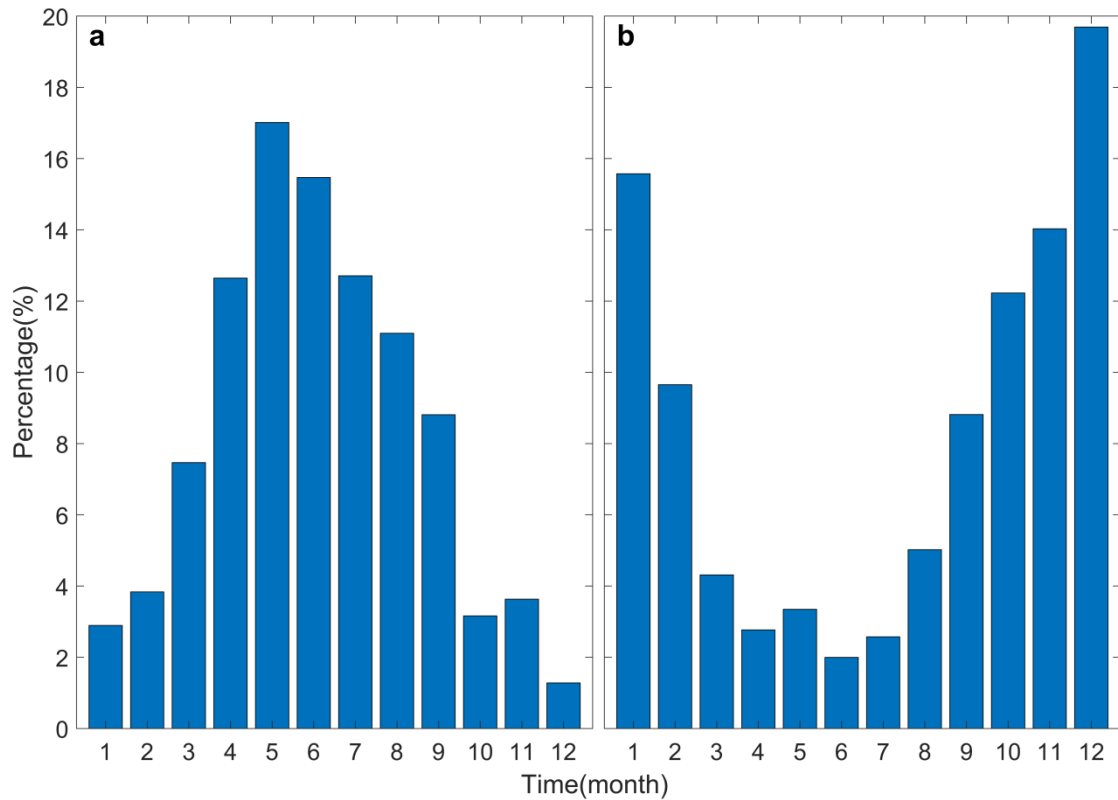
179

180 Figure 3. Time series of intensity index of counter-rotating eddy pair in LS (a). Red dotted line
 181 above (below) represents the sum (difference) of one time the standard deviation and the average
 182 value of the time series. Composition of SSHA for positive (b) and negative (c) intensity-index
 183 days. SSHA interval is 0.02 m. Figure based on HYCOM data.

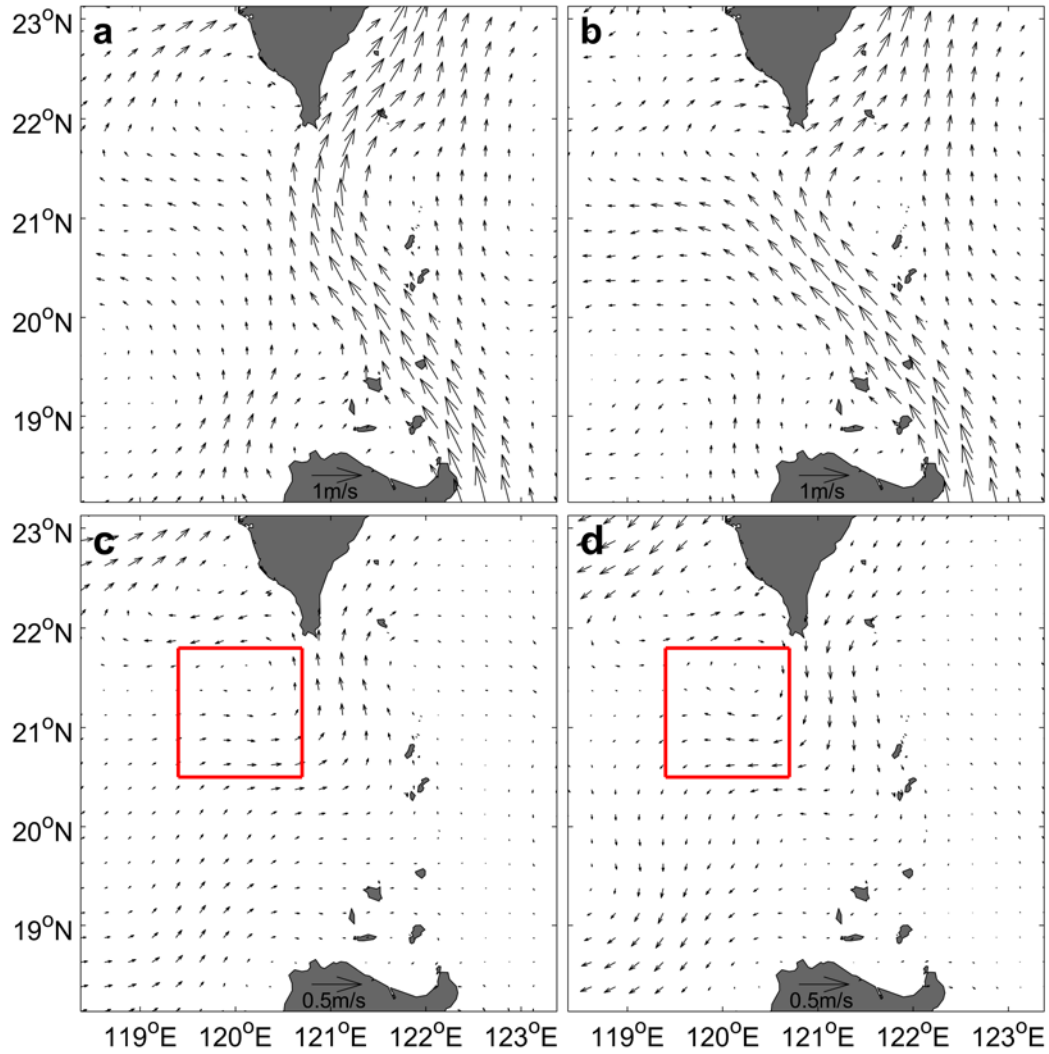
184 3.2 Seasonal variation of counter-rotating eddy pair in LS

185 We counted the temporal distribution of the positive and negative intensity index values in a
 186 statistical sense. Figure 4a (4b) shows that most of the AE (CE) mode of the instances of the
 187 counter-rotating eddy pair occur in the summer (winter) half of the year. The first two months with
 188 the highest incidences of the AE (CE) mode are May and June (December and January), and their
 189 occurrence rates are 17.01% and 15.47% (19.69% and 15.57%), respectively. We constructed the
 190 geostrophic current in May and June (Figure 5a) and in December and January (Figure 5b). The
 191 patterns of the Kuroshio Current in Figures 5a and 5b exhibit as the “Leap” and “Loop” patterns

192 of the Kuroshio in the LS, which illustrates that the Leap and Loop patterns of the Kuroshio
 193 contribute to the occurrence of the AE and CE modes, respectively, of the counter-rotating eddy
 194 pair. Figure 5c (5d) shows that the geostrophic current anomaly in the northern LS is northward
 195 (southward). It produces positive (negative) vorticity through horizontal velocity shear on the west
 196 side of the LS, and then contributes to the formation of a CE (an AE) on the west side of the LS.
 197 We discuss the dynamic mechanism of the counter-rotating eddy-pair phenomenon in detail in
 198 Section 3.3.



199
 200 Figure 4. Seasonal distribution of occurrence rate for positive (a) and negative (b) intensity
 201 indexes.



202

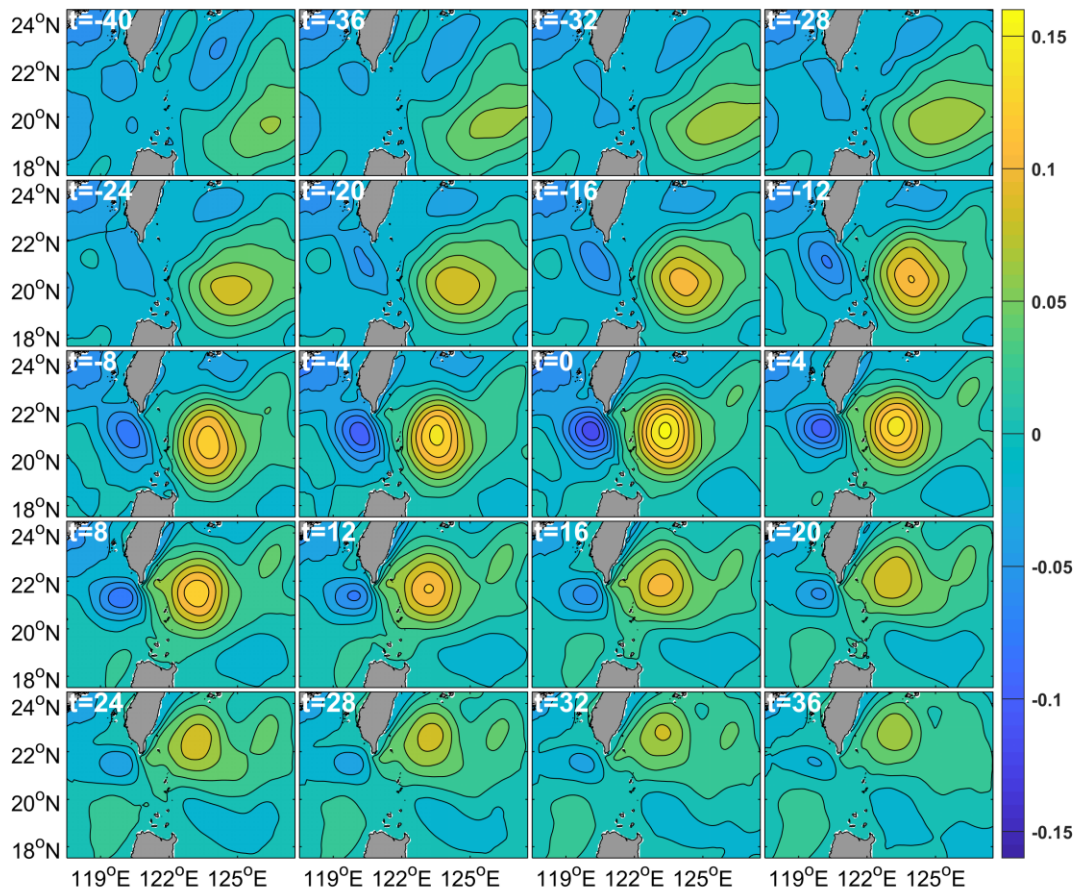
203 Figure 5. Climatic distributions of geostrophic current in May and June (a) and in December and
 204 January (b), and of geostrophic current anomaly in May and June (c) and in December and
 205 January (d). Red boxes in c and d outline 20.5–21.8°N, 119.4–120.7°E, which represent the
 206 position of mesoscale eddies on west side of LS. Figure based on CMEMS data.

207 3.3 Evolution of counter-rotating eddy pair in LS

208 Figure 6 shows the spatial evolution of the AE mode of the counter-rotating eddy pair in the
 209 LS. It shows that at the beginning, for example, at $t = -24$, there is a weak AE far from the east
 210 side of the LS, but no CE on the west side of the LS. From $t = -20$ to $t = 0$, as the AE in the NWP
 211 approaches the northern LS, a CE gradually forms on the west side of the LS. At $t = 0$, the AE

212 mode reaches its maximum. Then, from $t = 4$ to $t = 36$, as the AE in the NWP gradually moves
213 away from the northern LS, the CE on the west side of the LS gradually weakens until it finally
214 dies out.

215 The growth and weakening of a mesoscale eddy must be accompanied by a change in its
216 relative vorticity. Figure 7a shows that as the AE on the east side of the LS approaches and then
217 moves away from the northern LS, its relative vorticity initially decreases and then increases,
218 while the relative vorticity of the corresponding CE on the west side of the LS initially increases
219 and then decreases. The maximum negative (positive) value of the time series of the AE (CE) on
220 the east (west) side of the LS reaches $-4.2 \times 10^{-6} \text{ s}^{-1}$ ($3.6 \times 10^{-6} \text{ s}^{-1}$). These time series have good
221 correspondence and their correlation coefficient is -0.97 at the 95% confidence level. Therefore,
222 the temporal variations in the relative vorticity in Figure 7a verify the evolution of the AE mode of
223 the counter-rotating eddy pair in the LS.



224

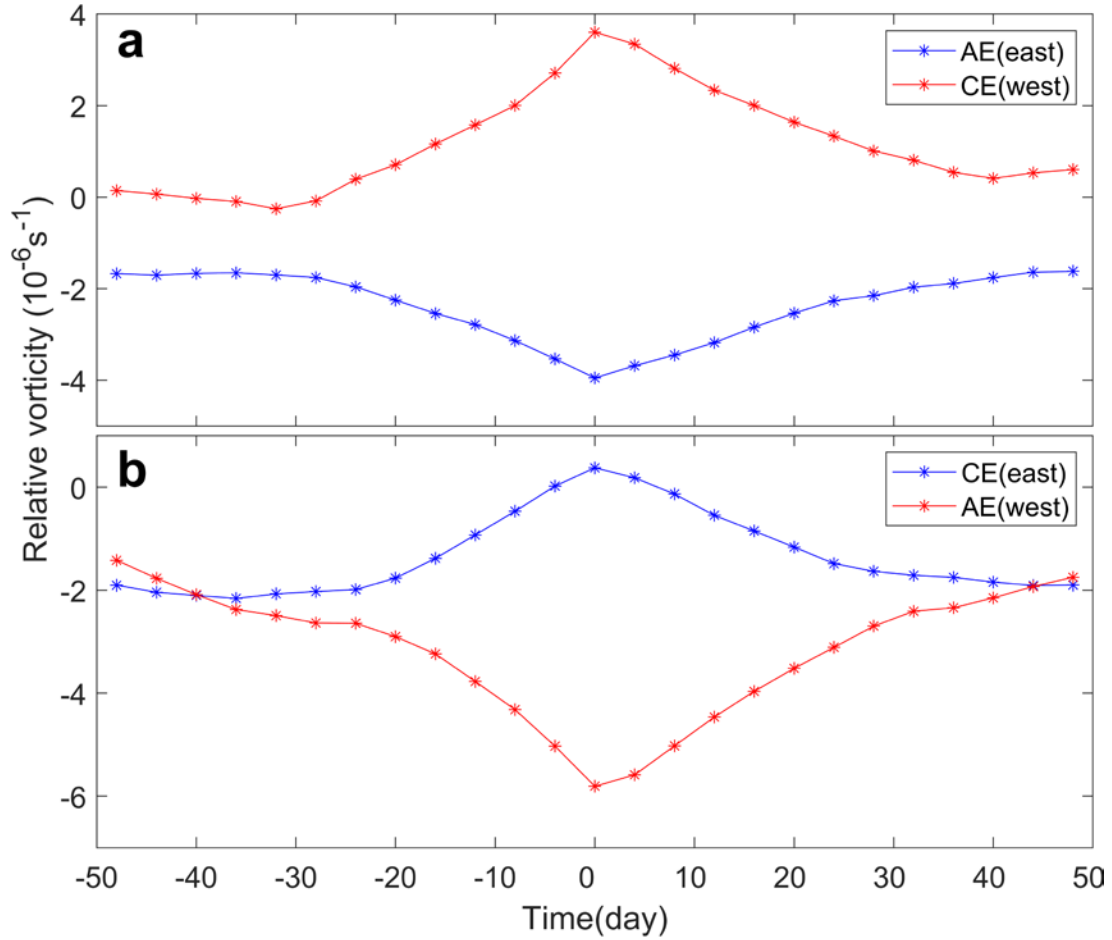
225 Figure 6. Evolution of AE mode of counter-rotating eddy pair in LS based on HYCOM data.

226 Contours and shading both represent SSHA (units of m). SSHA interval is 0.02 m. t value in the

227 top left-hand corner of each panel denotes the days before (negative value) or after (positive value)

228 AE mode of counter-rotating eddy pair reached the maximum (t=0). t = 0 corresponds to the time

229 of Figure 3b.



230

231 Figure 7. Distribution of relative vorticity in area bordered by red boxes in Figure 2. Panel a,
 232 relative vorticity of AE mode over time. Blue (red) line represents time series of relative vorticity
 233 of AE (CE) on east (west) side of LS, which corresponds to Figure 6. Panel b, relative vorticity of
 234 CE mode over time. Blue (red) line represents time series of relative vorticity of CE (AE) on east
 235 (west) side of LS, which corresponds to Figure 8. Figure based on HYCOM data.

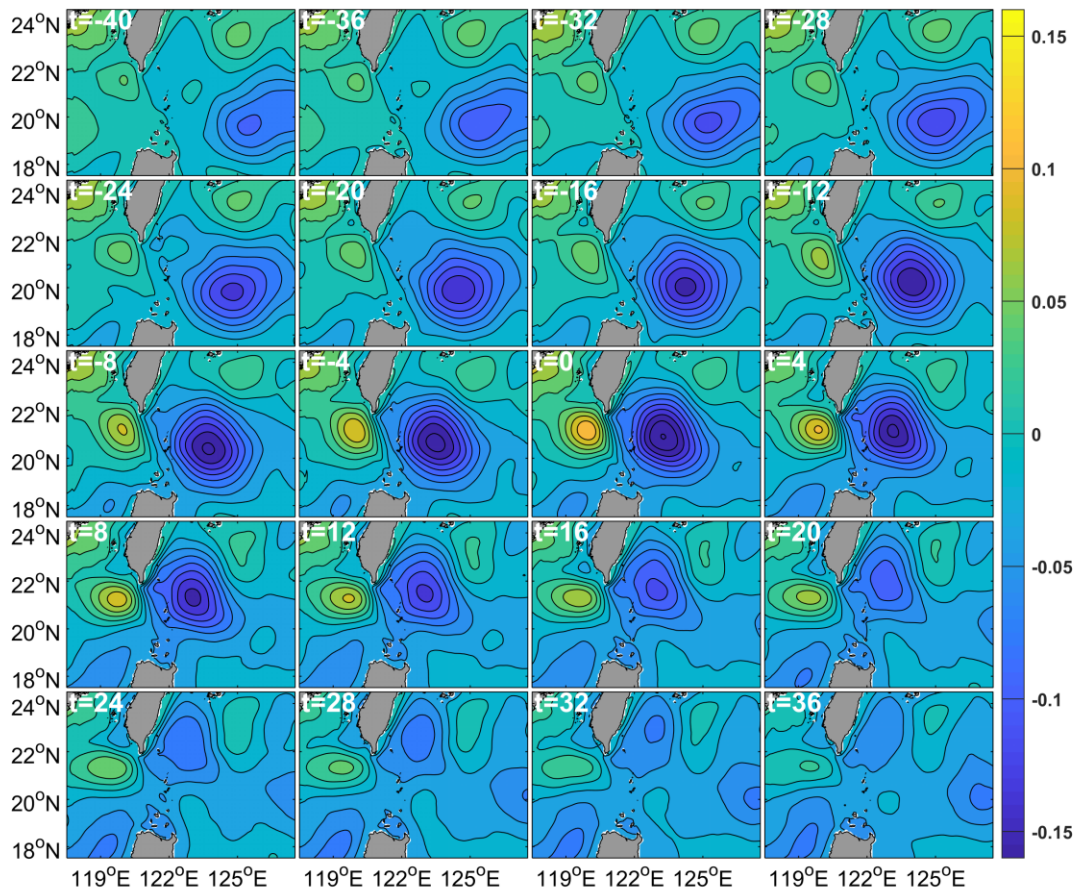
236 Figure 8 plots the CE mode of the counter-rotating eddy pair in the LS. It shows that at the
 237 beginning, for example, at $t = -32$, there is a weak CE far from the east side of the LS, but no AE
 238 on the west side of the LS. From $t = -28$ to $t = 0$, as the CE in NWP approaches the northern LS,
 239 an AE gradually forms on the west side of the LS. At $t = 0$, the CE mode of the evolution of the
 240 counter-rotating eddy pair reaches the maximum. Then, from $t = 4$ to $t = 36$, as the CE in the NWP

241 gradually moves away from the northern LS, the AE in the west side of the LS gradually weakens
242 until it finally dies out. Figure 7b plots the CE mode and shows that as the CE on the east side of
243 the LS approaches and moves away from the northern LS, its relative vorticity initially increases
244 and then decreases, while the relative vorticity of the corresponding AE on the west side of the LS
245 initially decreases and then increases. The maximum positive (negative) value of the time series of
246 the CE (AE) on the east (west) side of the LS can reach $0.48 \times 10^{-6} \text{ s}^{-1}$ ($-6.7 \times 10^{-6} \text{ s}^{-1}$). These time
247 series have good correspondence and their correlation coefficient is -0.96 at the 95% confidence
248 level. Therefore, the temporal variations in the relative vorticity in Figure 7b verify the evolution
249 of the AE mode of the counter-rotating eddy pair in the LS. The evolution of the AE and CE
250 modes of the counter-rotating eddy pair in the LS is also reflected by the satellite observations
251 (Figures 9 and 10).

252

253

254



255

256 Figure 8 Evolution of CE mode of counter-rotating eddy pair in LS based on HYCOM data.

257 Contours and shading both represent SSHA (units of m). SSHA interval is 0.02 m. t in the top

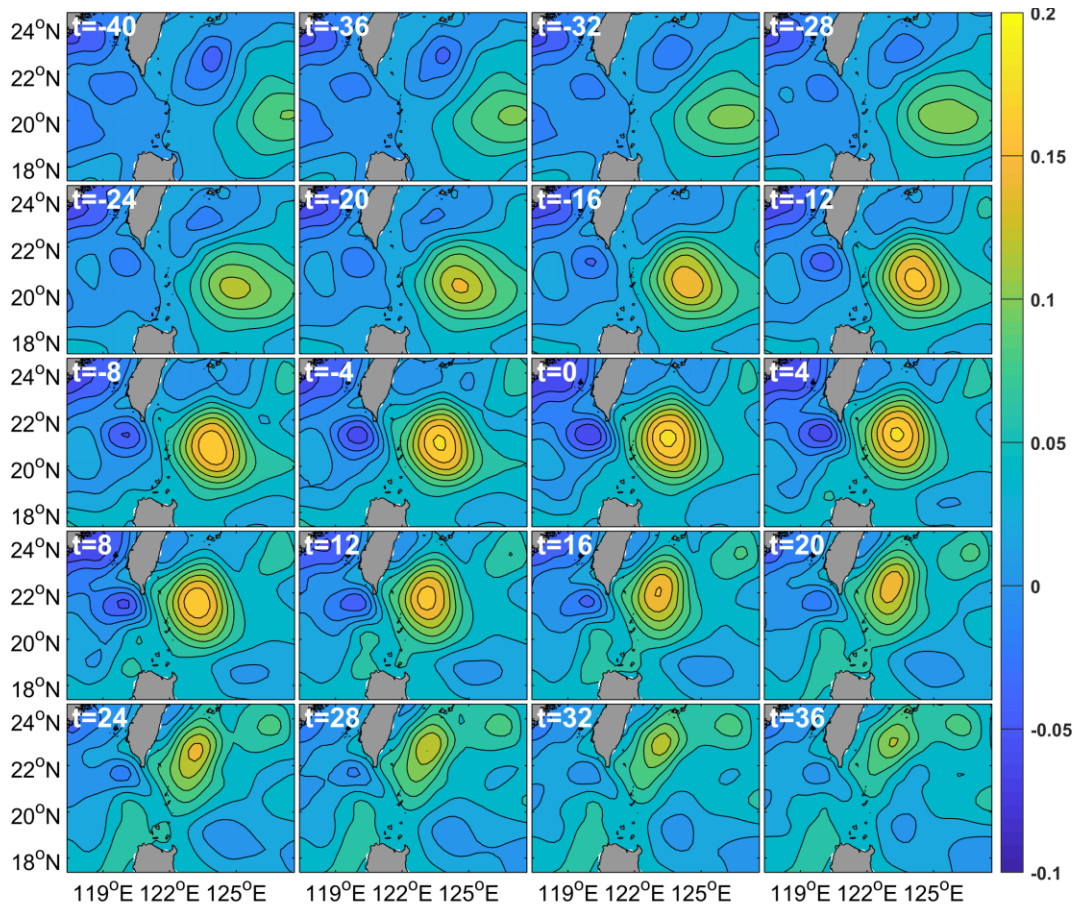
258 left-hand corner of each panel denotes the days before (negative value) or after (positive value) the

259 CE mode of the counter-rotating eddy pair reached the maximum (t=0). t = 0 corresponds to time

260 of Figure 3b.

261

262



263

264 Figure 9 Evolution of AE mode of counter-rotating eddy pair in LS based on CMEMS data.

265 Contours and shading both represent SSHA (units of m). SSHA interval is 0.02 m. t in the top

266 left-hand corner of each panel denotes days before (negative value) or after (positive value) the

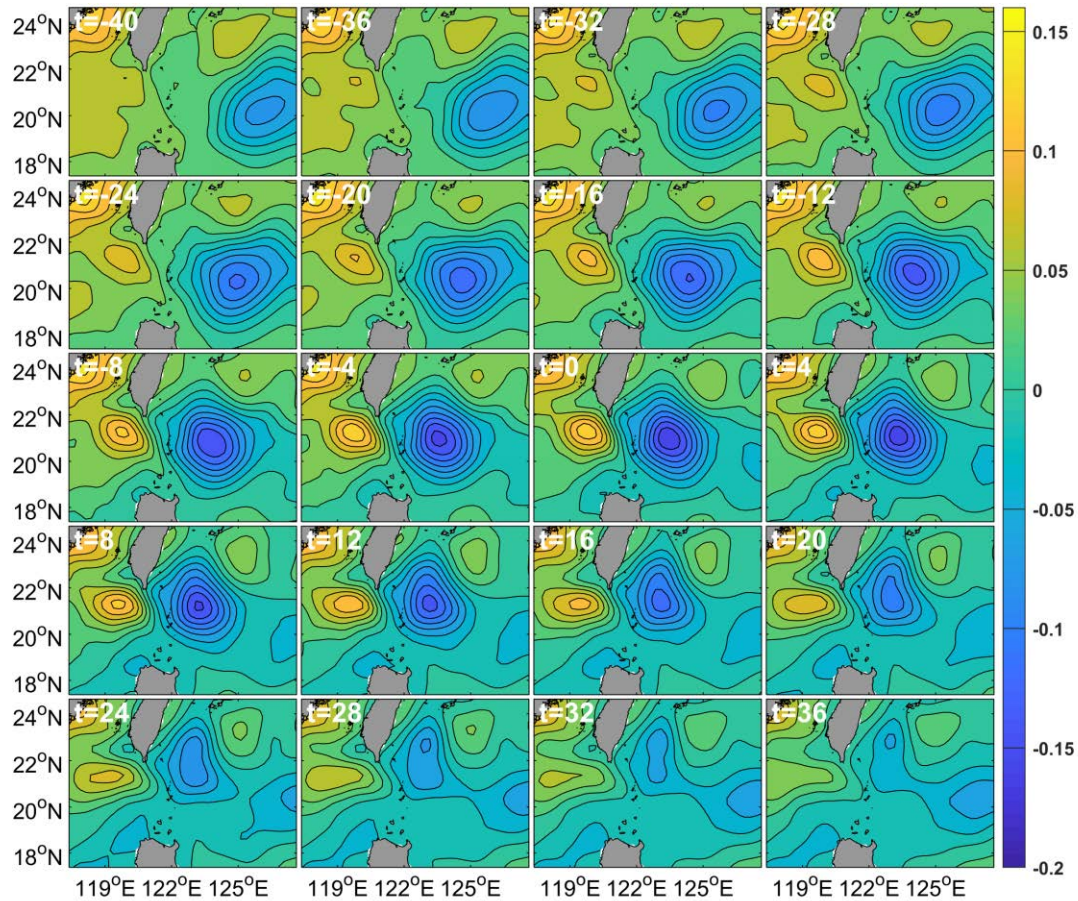
267 AE mode of counter-rotating eddy pair reached the maximum ($t=0$). $t = 0$ corresponds to time of

268 Figure 3b.

269

270

271



272

273 Figure 10 Evolution of CE mode of counter-rotating eddy pair in LS based on CMEMS data.

274 Contours and shading both represent SSHA (units of m). SSHA interval is 0.02 m. t in the top

275 left-hand corner of each panel denotes days before (negative value) or after (positive value) the

276 CE mode of counter-rotating eddy pair reached the maximum (t=0). t = 0 corresponds to time of

277 Figure 3b.

278 3.4 Formation mechanism of counter-rotating eddy pair in LS

279 Zhang *et al.* (2017) reported that CEs mainly formed due to the barotropic instability caused

280 by horizontal velocity shear of the Kuroshio Loop current southwest of Taiwan Island. Huang *et al.*

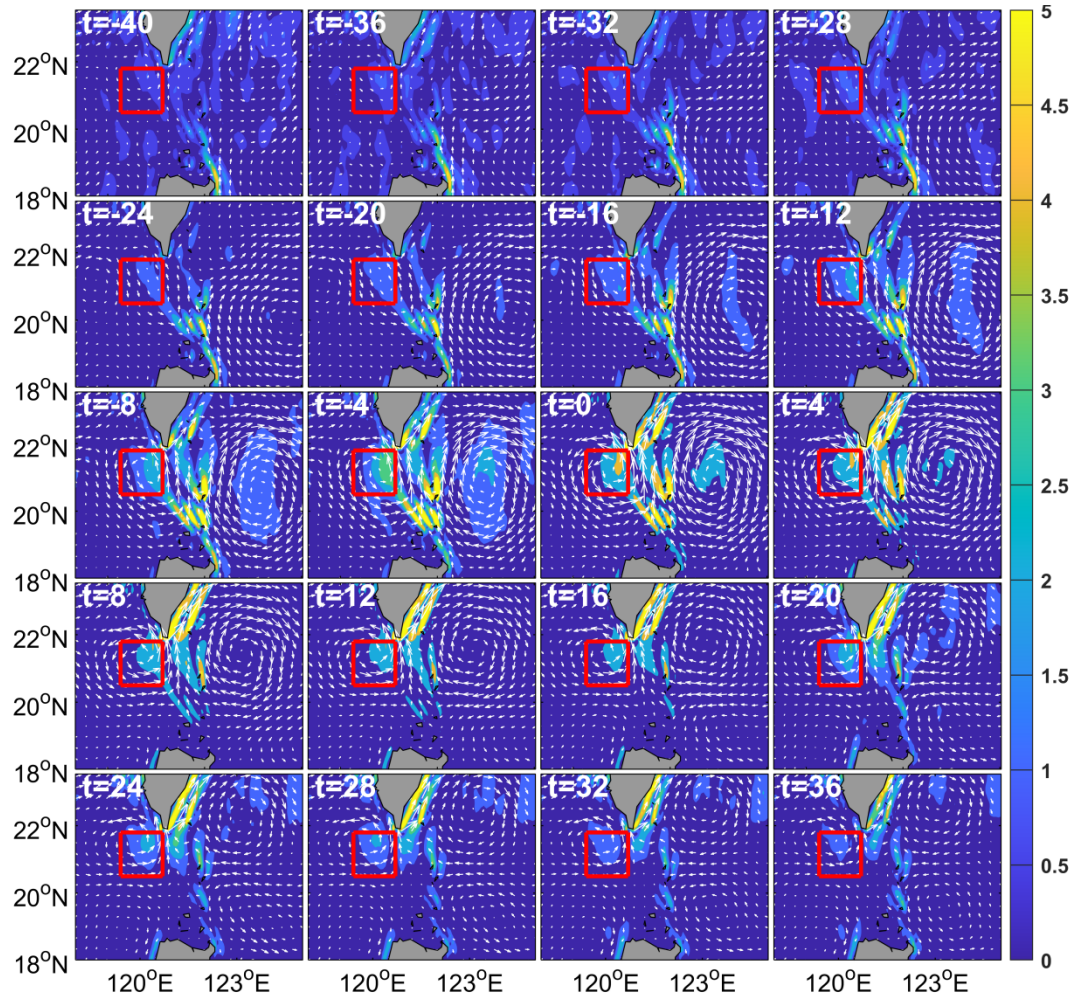
281 (2019) discovered that an AE from the NWP caused a CE to form on the west side of the LS via

282 horizontal velocity shear. In addition, Figures 3b and 3c show that the dense contour of the SSHA

283 means that there are strong current anomalies and thus strong horizontal velocity shear at the

284 junction of the AE and CE. Therefore, we investigated the role of horizontal velocity shear in the
285 formation of a counter-rotating eddy in the LS.

286 Because meridional horizontal velocity shear is weak, we only show the zonal velocity shear.
287 Figure 11 shows that from $t = -40$ to $t = 0$, as the AE on the east side of the NWP gradually
288 approaches the northern LS, the absolute value of the zonal horizontal velocity shear ($\frac{\partial v}{\partial x}$)
289 gradually increases, and a CE gradually forms and strengthens on the west side of the LS. From t
290 $= 0$ to $t = 36$, as the AE gradually moves away from the northern LS, the absolute value of the
291 zonal horizontal velocity shear gradually decreases, and the CE on the west side of the LS
292 gradually weakens. Figure 12 plots the CE mode of the counter-rotating eddy pair in the LS and
293 shows a similar corresponding evolution process. This demonstrates that there is good
294 correspondence between the zonal horizontal velocity shear and evolution process of the
295 counter-rotating eddy pair.



296

297 Figure 11 Evolution process of absolute value of zonal horizontal velocity shear ($\frac{\partial v}{\partial x}$) for AE

298 mode of counter-rotating eddy pair in LS based on HYCOM data. Shading represents zonal

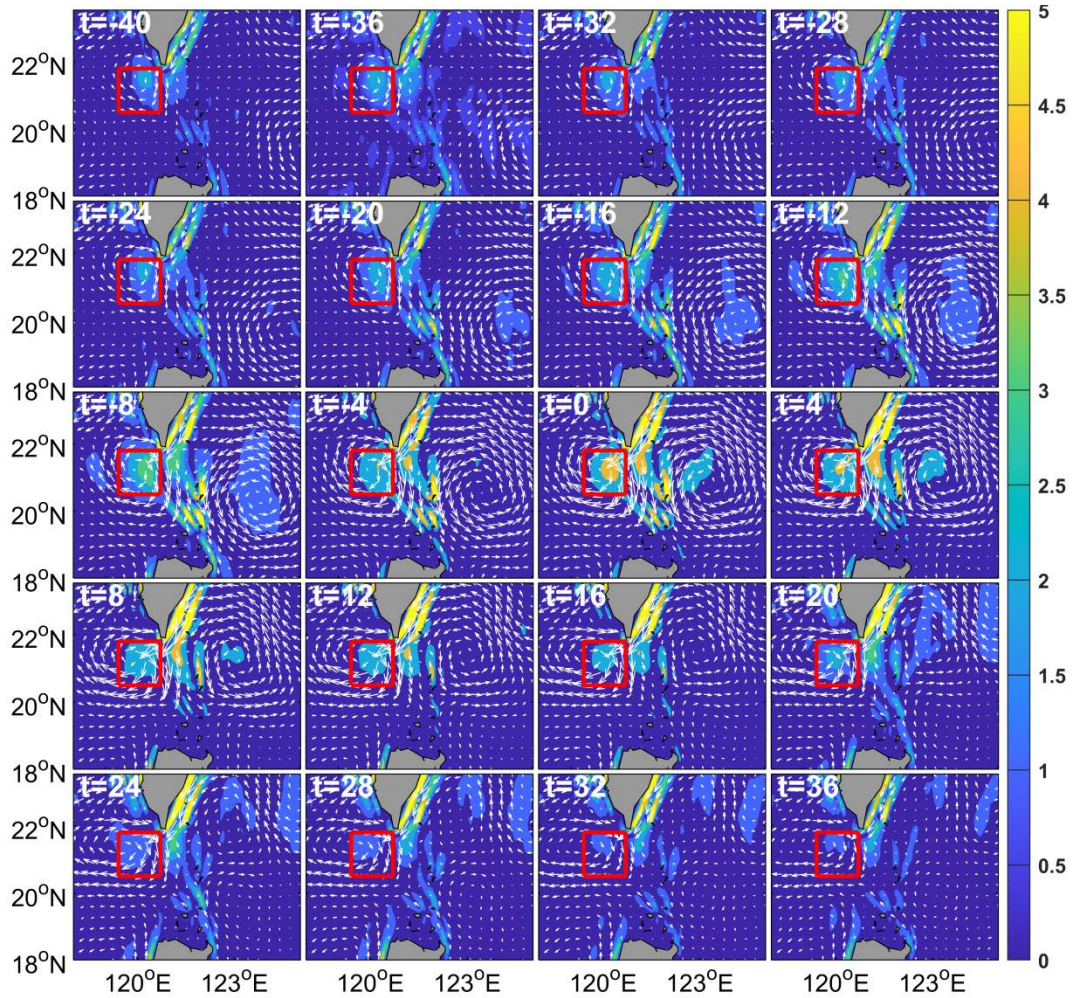
299 horizontal velocity shear (units of 10^{-6} s^{-2}). Vector represents the current anomaly. t in the top

300 left-hand corner of each panel denotes days before (negative value) or after (positive value) the

301 AE mode of counter-rotating eddy pair reached the maximum ($t = 0$). $t = 0$ corresponds to time of

302 Figure 3b. Red boxes on west side of LS cover $20.5\text{--}21.8^\circ\text{N}$, $119.4\text{--}120.7^\circ\text{E}$ and represent

303 location of CE on west side of LS.



304

305 Figure 12 Evolution process of absolute value of zonal horizontal velocity shear ($\frac{\partial v}{\partial x}$) for CE

306 mode of counter-rotating eddy pair in LS based on HYCOM data. Shading represents zonal

307 horizontal velocity shear (units of 10^{-6} s^{-2}). Vector represents current anomaly. t in top left-hand

308 corner of each panel denotes days before (negative value) or after (positive value) the AE mode of

309 counter-rotating eddy pair reached the maximum (t = 0). Time t = 0 corresponds to time of Figure

310 3b. Red boxes on west side of LS cover 20.5-21.8°N, 119.4-120.7°E and represent the location of

311 CE on west side of LS.

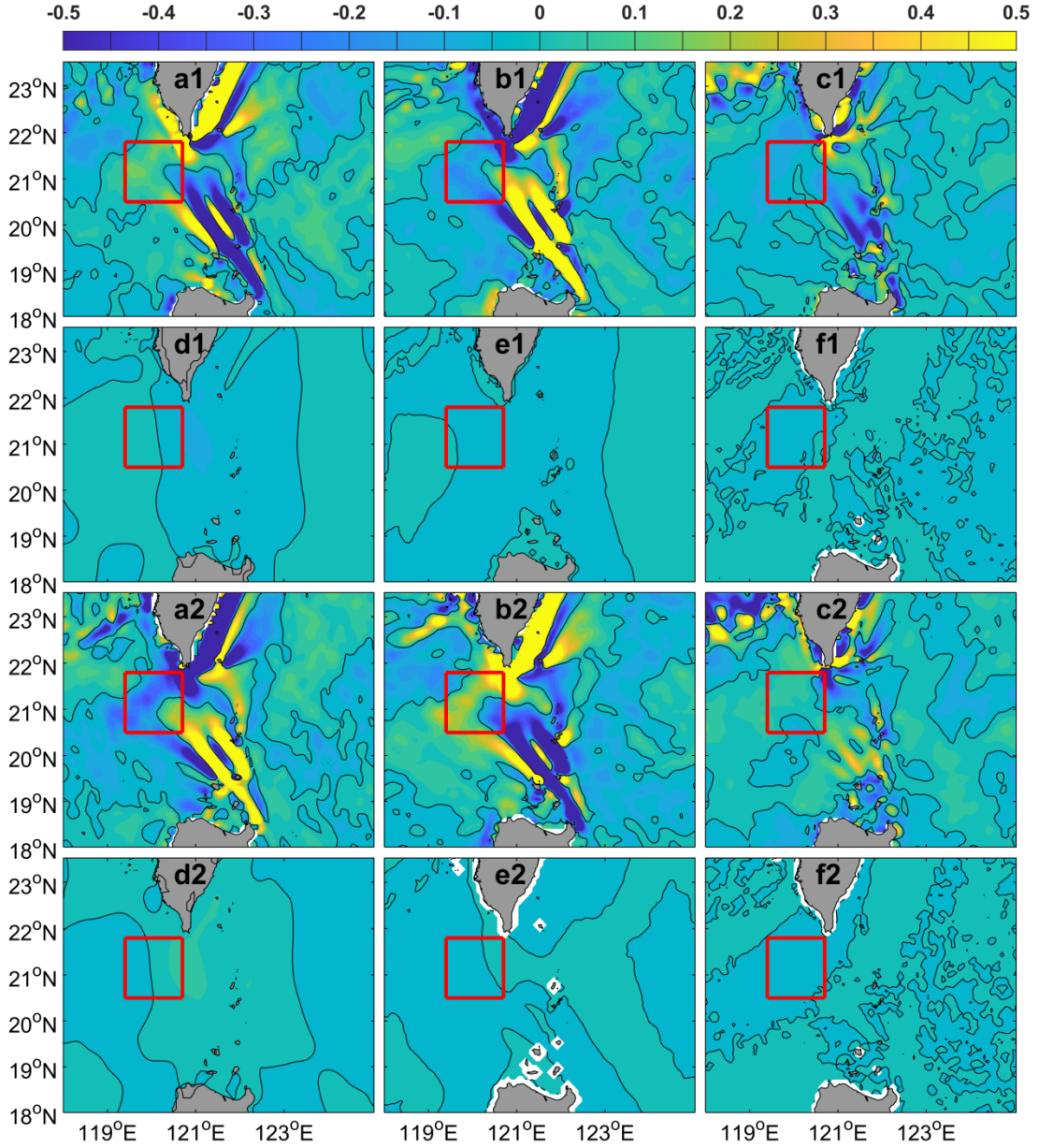
312 However, Figure 11 (12) shows that zonal horizontal velocity shear only occurs on the

313 right-hand side of the red box; that is, on the right-hand side of the CE (AE). How does the

314 horizontal velocity shear pass to the entire CE (AE)? To answer this question, we used the

315 vorticity budget equation. Figures 13a1–f1 plot the AE mode of the counter-rotating eddy pair and
316 show the respective contributions of the zonal advection, meridional advection, stretching, beta,
317 baroclinic, and diffusion terms of the vorticity budget equation. Compared to the stretching, beta,
318 baroclinic, and diffusion terms, the values of the zonal advection and meridional advection terms
319 in the red box are large. However, most of the values of the meridional advection term in the red
320 box are negative. Only positive vorticity advection can lead to formation of a CE, which suggests
321 that the zonal advection term is the main cause of CE formation in the red box. To further test this
322 conclusion, Figure 14a shows the correspondence between the relative vorticity anomaly and
323 zonal advection of the vorticity in the red box in Figure 13, illustrating that there is good
324 correspondence and their correlation coefficient is as high as 0.96 at the 95% confidence level.
325 Therefore, we conclude that the zonal advection term plays the most important role in vorticity
326 transport and contributes to the formation of the CE on the west side of the LS.

327 Figures 13a2–f2 are plots the CE mode of the counter-rotating eddy pair and shows that,
328 compared to the stretching, beta, baroclinic, and diffusion terms, the values of the zonal advection
329 and meridional advection terms in the red box are large. However, most of the values of the
330 meridional advection term in the red box are positive. Only negative vorticity advection can lead
331 to formation of an AE, which implies that the zonal advection term is the main cause of AE
332 formation in the red box. To further test this conclusion, Figure 14b shows the correspondence
333 between the relative vorticity anomaly and zonal advection of vorticity, illustrating that there is
334 good correspondence and their correlation coefficient is as high as 0.84 at the 95% confidence
335 level. Therefore, we conclude that the zonal advection term plays the most important role in
336 vorticity transport and contributes to the formation of the AE on the west side of the LS.



337

338 Figure 13. Vorticity budget equation for (a1–f1) AE mode of counter-rotating eddy pair and

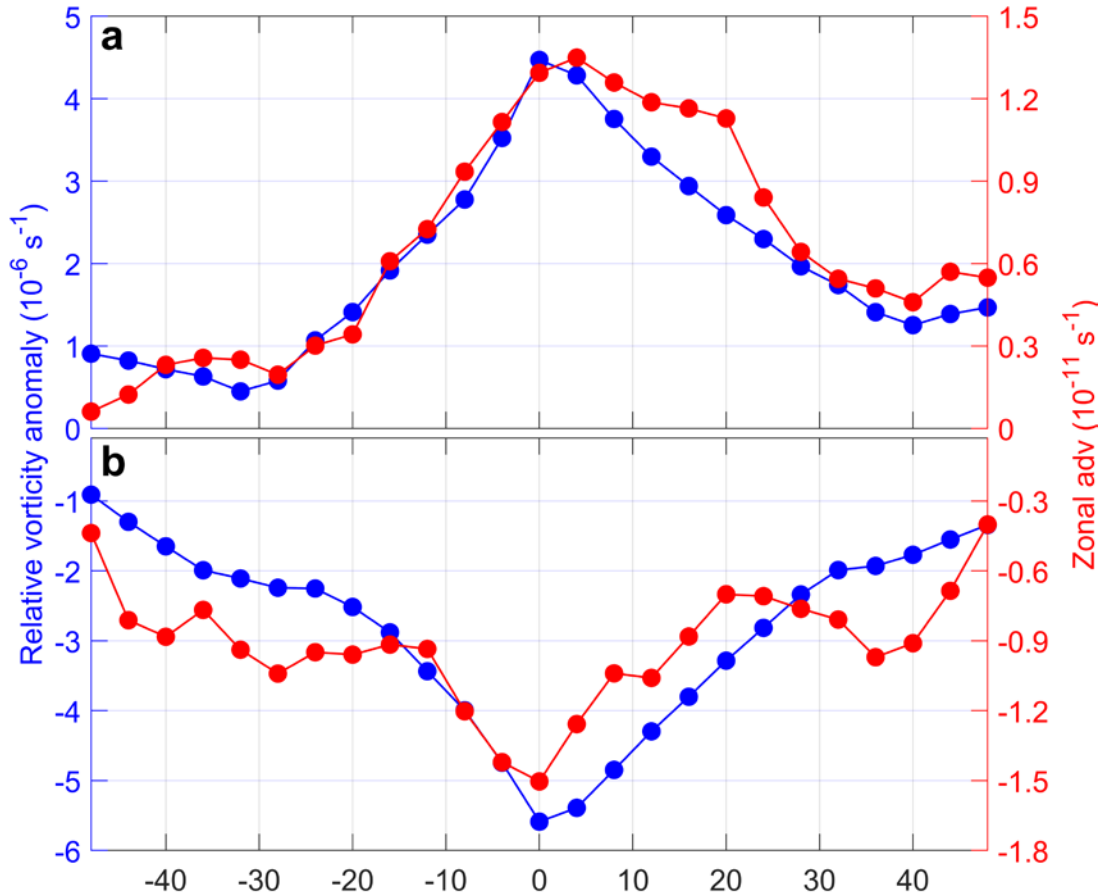
339 (a2–f2) CE mode of counter-rotating eddy pair. a1 and a2 represent the zonal advection term, b1

340 and b2 the meridional advection term, c1 and c2 the stretching term, d1 and d2 the beta term, e1

341 and e2 the baroclinic term, and f1 and f2 the diffusion term. Units are 10^{-10} s^{-2} . Red boxes on west

342 side of LS border cover $20.5\text{--}21.8^\circ\text{N}$, $119.4\text{--}120.7^\circ\text{E}$, and represent location of CE or AE on west

343 side of LS. Black solid line represents the zero contour. Figure based on HYCOM data.

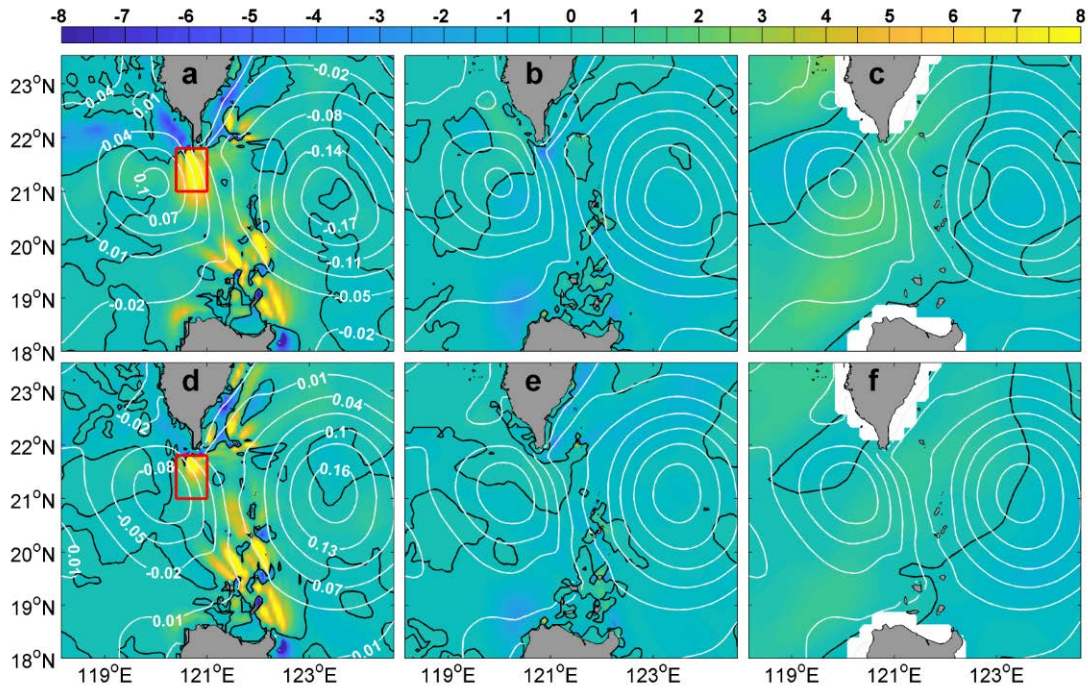


344

345 Figure 14. Distribution of relative vorticity anomaly and zonal advection of vorticity
 346 surrounded by red boxes in Figure 13 for AE (a) and CE (b) modes of counter-rotating eddy pair
 347 in LS.

348 It was mentioned above that the horizontal velocity shear caused by the mesoscale eddy on the
 349 east side of the LS is transported westward through zonal advection, resulting in the formation of a
 350 counter-rotating mesoscale eddy on the west side of the LS. Horizontal velocity shear will
 351 inevitably lead to barotropic instability. Now, we verify our conclusion from the perspective of
 352 energy. Figures 15a, 15b, and 15c show that, compared to the BC and WW values, the BT values
 353 in the LS are large and most of the values are positive, especially in the area surrounded by the red
 354 box in Figure 15a, which is the junction of the AE and CE. This means that the BT plays the most
 355 important role in formation of the AE on the west side of the LS.

356 Figures 15d, 15e, and 15f show the BT, BC, and WW, respectively, corresponding to the AE
 357 mode of the counter-rotating eddy pair in the LS. The description and dynamic mechanism of the
 358 AE mode are similar to those of the CE mode of the counter-rotating eddy pair in the LS, so the
 359 details will not be discussed here.



360
 361 Figure 15. BT based on HYCOM data ($10^{-5} \text{ m}^3 \text{ s}^{-3}$) represented by colors (a, d); BC based on
 362 HYCOM data ($10^{-5} \text{ m}^3 \text{ s}^{-3}$) represented by colors (b, e); WW based on CMEMS surface velocity
 363 data and NCDC wind data ($10^{-5} \text{ m}^3 \text{ s}^{-3}$) represented by colors (c, f). Red box borders 21°N–
 364 21.8°N, 120.4°E–121°E. White contours represent SSHA contours of. Panels a, b, and c (d, e, and
 365 f) plot CE (AE) mode of counter-rotating eddy pair in LS.

366 4 Discussion and conclusions

367 In this study, based on satellite observation data and HYCOM re-analysis data, the
 368 counter-rotating eddy pair in the LS is investigated. The phenomenon of counter-rotating eddy
 369 pairs is defined as the stage when an AE (a CE) in the NWP gradually approaches the northern LS,
 370 and a CE (an AE) forms on the west side of the LS. This phenomenon exhibits obvious seasonal

371 variation; that is, the AE mode mainly occurs in the summer half of the year, while the CE mode
372 mainly occurs in the winter half of the year. The mean durations of the AE and CE modes are both
373 approximately 70 d. The Leap and Loop patterns of the Kuroshio Current contribute to the
374 occurrence of the AE and CE modes, respectively, of counter-rotating eddy pairs. Based on the
375 vorticity budget equation and energy analysis, the dynamic mechanism of the occurrence of a
376 counter-rotating eddy pair is as follows. The AE (CE) in the NWP causes a positive (negative)
377 vorticity anomaly through horizontal velocity shear on the west side of the LS, and the positive
378 (negative) vorticity anomaly is transported westward by the zonal advection of the vorticity,
379 finally leading to the formation of a CE (an AE) on the west side of the LS. This conclusion is also
380 verified by barotropic instability based on the energy analysis.

381 When we investigated the question of how the horizontal velocity shear passes to the entire
382 CE or AE in Section 3.4, we found that the magnitudes of the meridional and zonal advection
383 terms are roughly the same. Because the meridional advection term has the opposite effect of CE
384 (AE) formation in the west side of the LS for the AE (CE) mode of the counter-rotating eddy pair,
385 we confirmed that the zonal advection term plays a main role in horizontal velocity shear
386 transportation. However, since the magnitude of the meridional advection term is very large, it
387 may play a role in the ocean dynamic process of the LS, which requires further study.

388 The results presented in this study are preliminary and several problems require further
389 research. The occurrence probability of a counter-rotating eddy pair in the LS must be determined.
390 The counter-rotating eddy pair phenomenon involves spatiotemporal variations in two mesoscale
391 eddies on both sides of the LS, and it is difficult to provide a quantifiable definition of this
392 phenomenon for a single event. For example, how far apart must the mesoscale eddies on the east

393 and west sides of the LS be to define them as a counter-rotating eddy pair. We preliminarily
394 calculated that the incidence of this phenomenon is approximately 5%.

395 Another problem to solve involves threshold of the NWP mesoscale eddies entering the SCS,
396 and what role the Kuroshio Current plays in the counter-rotating eddy-pair phenomenon in the LS.
397 In this study, our illustration of the counter-rotating eddy pair phenomenon does not include the
398 mean current field, which means that the influence of the Kuroshio Current is not considered.
399 However, the role of the Kuroshio in energy transfer is still worthy of further study. Numerical
400 simulations can be useful to address this issue. Our study provides new perspective on particle and
401 energy exchange, and further perfects the theory of particle and energy exchange between the SCS
402 and NWP.

403

404 **Acknowledges**

405 The authors would like to acknowledge several data sets used in this paper. Satellite remote
406 sensing geostrophic current data and sea level anomaly were obtained from the CMEMS, the
407 HYCOM reanalysis data were downloaded from HYCOM organization, the data set of wind was
408 provided by National Climate Data Center. Sea surface temperature data comes from Remote
409 Sensing System. This study was supported by National Natural Science Foundation of China (No.
410 41806019), Natural Science Foundation of Hainan Province (No. 121MS062), SCS ocean big data
411 center project of Sanya YZBSTC (No. SKJC-2022-01-001), Research Startup Funding from
412 Hainan Institute of Zhejiang University (No. HZY20210801), State Key Laboratory of Tropical
413 Oceanography, South China Sea Institute of Oceanology, Chinese Academy of Sciences (Project
414 No. LTO2011), Finance science and technology project of hainan province (No. ZDKJ202019),

415 Major science and technology project of Sanya YZBSTC (No. SKJC-KJ-2019KY03), High-level
416 Personnel of Special Support Program of Zhejiang Province, Funding (No. 2019R52045). We
417 thank the two anonymous reviewers for their constructive comments, and thank LetPub
418 (www.letpub.com) for its linguistic assistance during the preparation of this manuscript.

419

420 **Reference**

- 421 Huang Z, Zhuang W, Hu J, et al. Observations of the Luzon Cold Eddy in the northeastern South
422 China Sea in May 2017[J]. *Journal of Oceanography*, 2019, 75(5): 415-422.
- 423 Jing C, Li L. An initial note on quasi-stationary, cold-core Lanyu eddies southeast off Taiwan
424 Island[J]. *Chinese Science Bulletin*. 48(19): 2101-2107.
- 425 Kuo Y, Tseng Y. Influence of anomalous low-level circulation on the Kuroshio in the Luzon Strait
426 during ENSO[J]. *Ocean Modelling*, 2021, 159, 101559.
- 427 Ivchenko V O, Treguier A M, and Best S E. A kinetic energy budget and internal instabilities in the
428 fine resolution antarctic model, *Journal of Physical Oceanography*, 1997, 27:5-22.
- 429 Liu Y, Dong C, Guan Y, et al. Eddy Analysis in the Subtropical Zonal Band of the North Pacific
430 Ocean[J]. *Deep Sea Research Part I*, 2012, 68:54-67.
- 431 Lu J, Liu Q. Gap-leaping Kuroshio and blocking westward-propagating Rossby wave and eddy in
432 the Luzon Strait[J]. *Journal of Geophysical Research Oceans*, 2013, 118(3):1170-1181.
- 433 Muller P. Ertel's potential vorticity theorem in physical oceanography[J]. *Reviews of Geophysics*,
434 1995, 33(1):67-97.
- 435 Oey L Y. Loop Current and Deep Eddies[J]. *Journal of Physical Oceanography*, 2008, 38(7): 1426
436 -1449.
- 437 Pedlosky J. *Geophysical Fluid Dynamics*, 1987, 2nd ed., 710 pp., Springer, N. Y.

438 Pujol M, Françoise M. Product user manual for sea level SLA products. Copernicus Monitoring
439 Environment Marine Service (CMEMS), 2022, <https://doi.org/10.48670/moi-00148>.
440 Remote Sensing Systems (RSS): <https://www.remss.com/measurements/sea-surface-temperature/>.
441 Sun R, Ling Z, Chen C, et al. Interannual variability of thermal front west of Luzon Island in
442 boreal winter[J]. *Acta Oceanologica Sinica*, 2015, (34):108.
443 Sun R, Wang G, Chen C. The Kuroshio bifurcation associated with islands at the Luzon Strait[J].
444 *Geophysical Research Letters*, 2016a, 43(11):5768-5774.
445 Sun R, Gu Y, Li P, et al. Statistical characteristics and formation mechanism of the Lanyu cold
446 eddy[J]. *Journal of Oceanography*, 2016b, 72(4):641-649.
447 Sun R, Zhai F, Gu Y. The Four Patterns of the East Branch of the Kuroshio Bifurcation in the
448 Luzon Strait[J]. *Water*, 2018, 10(12).
449 Sun R, Zhai F, Zhang G, et al. Cold Water in the Lee of the Batanes Islands in the Luzon Strait[J].
450 *Journal of Ocean University of China*, 2020, 19(6):10.
451 Wallcraft A, Carroll S N, Kelly K A, et al. Hybrid Coordinate Ocean Model (HYCOM) Version
452 2.1 User's Guide. HYCOM consortium, 2003. [https://www.hycom.org/dataserver/gofs-3pt0](https://www.hycom.org/dataserver/gofs-3pt0/reanalysis)
453 /reanalysis.
454 Yang H, Wu L, Liu H, et al. Eddy energy sources and sinks in the South China Sea[J]. *Journal of*
455 *Geophysical Research Oceans*, 2013, 118(9):4716-4726.
456 Zhang Z, Zhao W, Tian J, et al. A mesoscale eddy pair southwest of Taiwan and its influence on
457 deep circulation[J]. *Journal of Geophysical Research Oceans*, 2013, 118(12):6479-6494.
458 Zhang Z, Zhao W, Tian J, et al. Spatial structure and temporal variability of the zonal flow in the
459 Luzon Strait[J]. *Journal of Geophysical Research Oceans*, 2015, 120(2).
460 Zhang Z, Zhao W, Qiu B, et al. Anticyclonic Eddy Sheddings from Kuroshio Loop and the

461 Accompanying Cyclonic Eddy in the Northeastern South China Sea[J]. Journal of Physical
462 Oceanography, 2017, 47(6):1243-1259.

463 Zhang H M, Reynolds R W, Bates J J, et al. Blended and gridded high resolution global sea
464 surface wind speed and climatology from multiple satellites: 1987-present. American
465 Meteorological Society 2006 Annual Meeting, Vol. 2. [https://www.ncei.noaa.gov/products](https://www.ncei.noaa.gov/products/blended-sea-winds)
466 /blended-sea-winds

467

468

469

470